AIAA 2003-0481

Helicity in Supercritical Temporal Mixing Layers

Nora Okong'o and Josette Bellan
Jet Propulsion Laboratory
California Institute of Technology
Pasadena CA 91109-8099

41st AIAA Aerospace Sciences Meeting and Exhibit
January 6–9, 2003/Reno, NV

Helicity in Supercritical Temporal Mixing Layers

Nora Okong'o[*] and Josette Bellan[†]

Jet Propulsion Laboratory
California Institute of Technology
Pasadena CA 91109-8099

Databases of transitional states obtained from Direct Numerical Simulations (DNS) of temporal, supercritical mixing layers for two species systems, O_2/H_2 and C_7H_{16}/N_2, are analyzed to elucidate species-specific turbulence aspects. The layers initially host four vortices whose double pairing is induced by perturbing the layers. The DNS were performed for the two species systems at similar reduced pressure (ratio of the pressure to the critical pressure) for the heavier fluid and similar initial momentum ratio, but at different initial density stratification. The relative helicity density shows that the velocity and vorticity are most likely orthogonal, negatively aligned or positively aligned; however, the preferred alignment varies among the layers, depending on species system and initial conditions. At the transitional states, the helicity-density (vorticity/velocity scalar product) has greater symmetry between positive and negative regions for C_7H_{16}/N_2 layers, which is also observed for the relative helicity density. The helicity density exhibits more intense activity for the C_7H_{16}/N_2 layers, which is attributed to the increased turbulence that results both from thermodynamic differences between the two species systems and from the lower initial density stratification of the C_7H_{16}/N_2 layers. The helicity (volume integral of helicity-density) variation is due to competition between baroclinic and viscous effects, and varies non-monotonically during each layer evolution. The influence of the pressure gradient on the helicity evolution shows the importance of supercritical thermodynamics in the dynamical characteristics of supercritical temporal mixing layers.

Introduction

Supercritical fluids are of great interest in extraction processes as well as in propulsion devices such as advanced gas-turbine and diesel engines, and liquid rockets. The performance of these devices depends on the efficiency of fluid disintegration and turbulent mixing, which may occur under supercritical conditions. A fluid is here defined to be in a supercritical state when it is at a thermodynamic pressure, p, or temperature, T, exceeding its critical (subscript c) value,[1] p_c or T_c. Therefore, in the supercritical regime there is no longer the possibility of a two phase (i.e. gas/liquid) region.[2] For mixtures, both p_c and T_c depend on the composition. The present interest is in fluid mixtures at high pressures that are supercritical for the pure species. Past the critical point of the fluid (where material surfaces no longer exist), the disintegration of fluid jets displays an aspect that Chehroudi et al.[3] call 'fingers', or 'comb-like structures' at transcritical conditions, which have an increasingly gaseous appearance with increasing p. Similar experimental evidence was produced by Mayer et al.[4,5] for O_2 disintegration. For supercritical free N_2 jets, the experiments of Oschwald and Schik[6] showed sharp density profiles, indicating

the occurrence of sharp density gradients. Results from Direct Numerical Simulations (DNS) showed that such regions of high density-gradient-magnitude exist in both pre-transitional[7] and transitional[8,9] mixing layers, arising both from the initial density stratification as well as from mixing. However, there is still uncertainty regarding the influence of supercritical thermodynamics on the dynamical characteristics of the flow.[10]

An important dynamical characteristic of the flow is the helicity density, $(\mathbf{u} \cdot \omega)$, where $\mathbf{u}$ is the velocity and $\omega = \nabla \times \mathbf{u}$ is the vorticity. The helicity density is the velocity magnitude multiplied by the projection of the vorticity in the flow direction, and is null for a two-dimensional flow. The volume integral of the helicity density is the helicity, $H = \int_V (\mathbf{u} \cdot \omega) dV$. The helicity has special significance when the flow consists of closed vortex lines, in which case the helicity is a measure of topological aspects of a flow, specifically, knottedness.[11,12] According to Moffatt,[11] for barotropic and inviscid flow in a bounded volume, H is invariant. For decaying nearly isotropic turbulence, where H was initially null and random, Shtilman et al.[13] found that viscous effects could generate helicity, whereas Rogers and Moin[14] concluded that for homogeneous turbulence with zero initial helicity, viscosity did not appear to generate H; note that whereas viscosity is a sink for $(\mathbf{u} \cdot \mathbf{u})$ and $(\omega \cdot \omega)$, it can be either a source or sink for H. A third helicity characteristic is the relative helic-

ity density, $\cos(\mathbf{u},\omega) = (\mathbf{u} \cdot \omega)/(|\mathbf{u}|\,|\omega|)$, which measures the vorticity-velocity alignment. For decaying, nearly isotropic turbulence, Shtilman et al.[13] showed that $\mathbf{u}$ and ω evolved a manner that rendered the probability density function (PDF) of $\cos(\mathbf{u},\omega)$ to be highest for ± 1, that is, $\mathbf{u}$ and ω aligned. This result was confirmed by Pelz et al.[15] for unforced turbulent flows. Additionally, Pelz et al.[16] showed that for specific turbulent flows (plane Poiseuille and Taylor-Green vortex), this alignment tends to coincide with regions of low turbulent kinetic energy dissipation, whereas in regions of high turbulent kinetic energy dissipation, the magnitude of $\cos(\mathbf{u},\omega)$ was evenly distributed. Rogers and Moin[14] studied the relative helicity density of the disturbance flow for incompressible homogeneous turbulence and turbulent channel flow and concluded that there is only a weak correlation between the relative orientation of the velocity and vorticity. Finally, the experimental results of Wallace et al.[17] from a turbulent boundary layer, a turbulent two-stream mixing layer and a turbulent grid flow did not support the conclusion that there is a high probability of $\mathbf{u}$ and ω being aligned; slight alignment was observed only in the shear flow. The experimental results, however, did support to some extent the aforementioned conclusions from numerical simulations regarding the correlation between regions of aligned $\mathbf{u}$ and ω and those of small turbulent kinetic energy dissipation. These, sometimes apparently contradictory, conclusions regarding the alignment of $\mathbf{u}$ and ω indicate that the relative helicity density should be studied in different types of flows, and for different initial conditions in order to extract more definitive results.

In this paper, we conduct further investigations into DNS databases of supercritical temporal mixing layers, leading to insights into helicity under supercritical conditions. For the conditions of this study, the mixing layers have initially a strong density stratification between the two free streams, each of which is composed of a single species, and the layers are perturbed to induce the evolution of coherent structures. The databases consist of oxygen/hydrogen (O_2/H_2) mixing layers[8] as well as heptane/nitrogen (C_7H_{16}/N_2) layers;[9] critical properties for these species are listed in Table 1. The C_7H_{16}/N_2 system is adopted as being representative of an air/hydrocarbon mixture in gas turbine and diesel engines, which is currently too complex for detailed fundamental simulations, whereas the O_2/H_2 system is relevant to liquid rocket engines. The databases include simulations at different initial conditions for each species system, in a thermodynamic regime of interest for the practical situation. This paper is organized as follows: First, we summarize the DNS methodology including the governing equations, the flow configuration and boundary conditions. The initial conditions are then discussed to highlight the issues in determining meaningful regimes for comparisons between the O_2/H_2 and C_7H_{16}/N_2 systems given their disparate mixture thermodynamics. The comparisons made among layers focus on the helicity evolution and the helicity aspects of each layer at the transitional state, and they consider the impact of the thermodynamics of each species system on the helicity characteristics. Finally, the results are summarized and conclusions are presented.

DNS methodology

A detailed description of the DNS methodology has been given by Miller et al.[7] and Okong'o and Bellan[8] for C_7H_{16}/N_2 layers and by Okong'o et al.[9] for the O_2/H_2 layers. Those descriptions are summarized here to emphasize aspects of the formulation that are different from the typical low-pressure situation. The DNS governing equations consist of conservation equations, the equation of state (EOS) and transport property relations, which are solved for specific initial and boundary conditions, using a suitably accurate numerical scheme.

Conservation equations

The conservation equations originate in Keizer's[18] fluctuation-dissipation (FD) theory which is consistent with non-equilibrium thermodynamics, converges to kinetic theory in the low-pressure limit and relates fluxes and forces from first principles. For a binary mixture, the conservation equations are

$$\frac{\partial \rho}{\partial t} + \frac{\partial (\rho u_j)}{\partial x_j} = 0, \tag{1}$$

$$\frac{\partial (\rho u_i)}{\partial t} + \frac{\partial (\rho u_i u_j + p\delta_{ij})}{\partial x_j} = \frac{\partial \tau_{ij}}{\partial x_j}, \tag{2}$$

$$\frac{\partial (\rho Y_\alpha)}{\partial t} + \frac{\partial (\rho Y_{\alpha 2} u_j)}{\partial x_j} = -\frac{\partial j_{\alpha j}}{\partial x_j}, \quad \alpha = 1, N \tag{3}$$

$$\frac{\partial (\rho e_t)}{\partial t} + \frac{\partial [(\rho e_t + p) u_j]}{\partial x_j} = -\frac{\partial q_{IKj}}{\partial x_j} + \frac{\partial \tau_{ij} u_i}{\partial x_j}, \tag{4}$$

where x is a Cartesian coordinate, t is time, ρ is the density, u_i is the ith component of the velocity, $e_t = e + u_i u_i/2$ is the total energy (i.e. internal energy, e, plus kinetic energy), Y_α is the mass fraction of species α and $\mathbf{j}_\alpha$ is its mass flux vector ($\sum_{\alpha=1}^{N} Y_\alpha = 1, \sum_{\alpha=1}^{N} j_{\alpha j} = 0$) for a mixture of N species. In the binary ($N = 2$) mixing layer configuration, the lighter (molar weight) species (subscript 1) will be in the upper stream, and the other species (subscript 2) will be in the lower stream. Furthermore, $\mathbf{q}_{IK}$ is the Irwing-Kirkwood (subscript IK) form of the heat flux vector (see Sarman and Evans[19]), and τ_{ij} is the Newtonian viscous stress tensor

$$\tau_{ij} = \mu \left[\frac{\partial u_i}{\partial x_j} + \frac{\partial u_j}{\partial x_i} - \frac{2}{3}\frac{\partial u_k}{\partial x_k}\delta_{ij} \right], \tag{5}$$

where δ_{ij} is the Kronecker delta function, and μ is the mixture viscosity that is in general a function of the

thermodynamic state variables. The mass flux and heat flux are given by

$$j_{2j} = -\left[j'_{2j} + (\alpha_{IK} - \alpha_h)Y_2 Y_1 \frac{\rho D}{T}\frac{\partial T}{\partial x_j}\right], \quad (6)$$

$$q_{IKj} = -\lambda'_{IK}\frac{\partial T}{\partial x_j} - \alpha_{IK}R_u T \frac{m}{m_2 m_1}j'_{2j}, \quad (7)$$

$$j'_{2j} = \rho D\left[\alpha_D\frac{\partial Y_2}{\partial x_j} + \frac{Y_2 Y_1}{R_u T}\frac{m_2 m_1}{m}\left(\frac{v_{,2}}{m_2} - \frac{v_{,1}}{m_1}\right)\frac{\partial p}{\partial x_j}\right], \quad (8)$$

$$\alpha_h = \frac{1}{R_u T}\frac{m_2 m_1}{m}\left(\frac{h_{,2}}{m_2} - \frac{h_{,1}}{m_1}\right). \quad (9)$$

The notation in eqs. 6 - 9 is as follows: D is the binary diffusion coefficient; α_D is the mass diffusion factor ($\alpha_D = 1$ for an ideal mixture); m_α is the molar mass of species α; $m = \sum_{\alpha=1}^{N} m_\alpha X_\alpha$ is the mixture molar mass where the molar fraction $X_\alpha = mY_\alpha/m_\alpha$; $v_{,\alpha} = (\partial v/\partial X_\alpha)_{T,p,X_\beta(\beta\neq\alpha)}$ is the partial molar volume and $h_{,\alpha} = (\partial h/\partial X_\alpha)_{T,p,X_\beta(\beta\neq\alpha)}$ is the partial molar enthalpy; $v = \sum_{\alpha=1}^{N} X_\alpha v_{,\alpha}$ is the molar volume related to the density by $v = m/\rho$; $h = \sum_{\alpha=1}^{N} X_\alpha h_{,\alpha}$ is the molar enthalpy; R_u is the universal gas constant and λ'_{IK} is a thermal conductivity defined from the transport matrix through

$$\lambda'_{IK} = \lambda + X_1 X_2\ \alpha_{IK}\ \alpha_{BK} R_u \rho D/m, \quad (10)$$

with $\lim_{p\to 0}\lambda = \lambda_{KT}$ as discussed in Harstad and Bellan,[20] where the subscript KT refers to Kinetic Theory. The transport coefficients associated with the Soret (in the molar fluxes) and the Dufour (in the heat flux) terms of the transport matrix are α_{BK} and α_{IK}, which are the thermal diffusion factors corresponding to the IK and the Bearman-Kirkwood (subscript BK) forms of the heat flux (see Sarman and Evans[19]). These transport coefficients are characteristic of each particular species pairs and they obey the relationship[20]

$$\alpha_{BK} = \alpha_{IK} - \alpha_h. \quad (11)$$

Additionally, $\lim_{p\to 0}\alpha_{IK} \neq \alpha_{KT}$ and $\lim_{p\to 0}\alpha_{BK} = \alpha_{KT}$.

Equation of state

The pressure is calculated from the well-known Peng-Robinson (PR) EOS, given T and the PR molar volume (v_{PR}), as

$$p = \frac{R_u T}{(v_{PR} - b_m)} - \frac{a_m}{(v_{PR}^2 + 2b_m v_{PR} - b_m^2)}, \quad (12)$$

where a_m and b_m are functions of T and X_α. At high pressures, v_{PR} may differ significantly from the actual molar volume v.[1] Both v_{PR} and the volume shift ($v_S = v - v_{PR}$) can be calculated from the PR EOS given p, T and X_α,[21] although for the C_7H_{16}/N_2 system v_S is negligible. All thermodynamic quantities,

including α_D, h, $C_p = (\partial h/\partial T)_{p,X}$ and the speed of sound (a_s), are calculated from the EOS using standard thermodynamic relations.[7-9] The calculation of p and T from the known conservative variables of Eqs. 1-4 uses an iterative scheme[9] for O_2/H_2 and an energy fit[8] for C_7H_{16}/N_2.

Transport coefficients

The viscosity, the Schmidt number (Sc) and the Prandtl number (Pr) were calculated from high-pressure single-species transport properties using mixing rules, as in Harstad and Bellan.[22] The calculated values were correlated, as summarized in Table 2, and these correlations are then used to compute the transport properties μ, D and λ. The temperatures T_1 (upper, H_2 or N_2, stream) and T_2 (lower, O_2 or C_7H_{16}, stream) correspond to the free-stream temperatures for mixing layer simulations. The value of the reference viscosity (μ_R) is determined by the specified value of the initial Reynolds number Re_0 (see eq. 15), chosen so as to enable the resolution of all relevant length scales. One of the thermal diffusion factors is specified, then the other is calculated from eq. 11.

Configuration, initial and boundary conditions

The temporally developing mixing layer configuration is depicted in Fig. 1 for O_2/H_2, as an example, showing the definition of the streamwise (x_1), cross-stream (x_2) and spanwise (x_3) coordinates. The layer is not symmetric in extent in the x_2 direction, to accommodate the larger layer growth in the lighter fluid (H_2 or N_2) side. The free-stream density (ρ_1 or ρ_2) is calculated for each pure species at its free-stream temperature (T_1 or T_2) and at the initial uniform pressure (p_0). The vorticity thickness is defined as $\delta_\omega(t) = \Delta U_0/(\partial \langle u_1\rangle/\partial x_2)_{max}$ where $\langle u_1\rangle$ is the (x_1, x_3) planar average of the streamwise velocity, and $\Delta U_0 = U_1 - U_2$ is the velocity difference across the layer. The simulation is initiated with four streamwise vortices, which pair twice to produce an ultimate vortex. The choice

$$U_1 = 2M_{c,0}a_{s_1}\left[1 + \left(\frac{a_{s_1}}{a_{s_2}}\right)\sqrt{\frac{\rho_1 Z_1}{\rho_2 Z_2}}\right]^{-1},$$

$$U_2 = -\sqrt{\frac{\rho_1 Z_1}{\rho_2 Z_2}}U_1, \quad (13)$$

was made with the intent of keeping the ultimate vortex stationary in the computational domain,[7] although the relations of Papamoschou and Roshko[23]

$$U_1 = 2M_{c,0}a_{s_1}\left[1 + \left(\frac{a_{s_1}}{a_{s_2}}\right)\sqrt{\frac{\rho_1}{\rho_2}}\right]^{-1}, U_2 = -\sqrt{\frac{\rho_1}{\rho_2}}U_1, \quad (14)$$

were also used for some simulations reported here. Here $M_{c,0}$ is the convective Mach number and $Z = p/(\rho T R_u/m)$ is the compression factor indicating de-

partures from perfect gas ($Z = 1$) behavior. The specification of $M_{c,0}$ therefore determines ΔU_0. Given the initial streamwise velocity profile u_1 based on U_1 and U_2, $(\partial \langle u_1 \rangle / \partial x_2)_{max}$ and hence $\delta_{\omega,0} \equiv \delta_\omega (0)$ are calculated. The specified value of the initial flow Reynolds number,

$$\text{Re}_0 = \frac{0.5 \left(\rho_1 + \rho_2 \right) \Delta U_0 \delta_{\omega,0}}{\mu_R} \tag{15}$$

is then used to calculate μ_R.

The simulations are started with error-function profiles for the mean streamwise velocity, mass fraction and temperature, upon which are imposed spanwise and streamwise vorticity perturbations[24,25] of strengths F_{2D} and F_{3D} respectively, whose streamwise (λ_1) and spanwise (λ_3) wavelengths are $\lambda_1 = C\delta_{\omega,0}$ and $\lambda_3 = 0.6\lambda_1$, where $C = 7.29$ is the most unstable wavelength for incompressible flow. For some simulations reported here, other values of C obtained from stability analyses[26] were also used: $C = 10.35$ or 10.61 for the most unstable wavelength for the O_2/H_2 layer (depending on the initial conditions) and $C = 4.57$ for the shortest (estimated) unstable wavelength for the C_7H_{16}/N_2 layer. The grid is chosen for all simulations so as to accommodate four wavelengths in the streamwise and spanwise directions, and the evolution of the layer is meant to encompass roll-up and two pairings of the initial spanwise vortices.

The boundary conditions are periodic in the streamwise and spanwise directions, and of outflow type for real gas in the cross-stream direction, as derived by Okong'o and Bellan.[27] The outflow type conditions are essential to maintain numerical stability since the initial perturbation causes large pressure waves that must be allowed out of the domain with minimal reflection.

Numerics

The conservation equations were numerically solved using a fourth-order explicit Runge-Kutta time integration and a sixth-order compact scheme with eighth-order filter for spatial derivatives;[28] for numerical stability, filtering is applied at interior points only. The computations were parallelized using three-dimensional domain decomposition and message passing, and an efficient parallel tridiagonal solver.[29]

Description of DNS databases

Free stream conditions

For databases produced from the DNS methodology described above, the intent is to compare simulations for the C_7H_{16}/N_2 and O_2/H_2 systems, in order to elucidate species-system-specific turbulence aspects. The thermodynamic initial conditions (p_0, T_1, T_2) are chosen for the C_7H_{16}/N_2 system to be in the regime of relevance to gas turbine and diesel engines (60 atm, $T_1 = 1000K$, $T_2 = 600K$), whereas those for the O_2/H_2

system are selected as close to the liquid rocket conditions as computationally feasible (100 atm, $T_1 = 600K$, $T_2 = 400K$ or 100 atm, $T_1 = 287K$, $T_2 = 235K$) because the quite different thermodynamic properties of the two mixtures (as encapsulated by their respective equations of state) do not permit the matching of the thermodynamic initial conditions (see discussion in Ref. 9). These three sets of free stream conditions, listed in Table 3, have quite similar momentum ratios $|\rho_2 U_2| / |\rho_1 U_1|$, and the initial pressure is such that the reduced pressure ($p_r \equiv p/p_c$) in the heavier fluids is similar. However, p_r is dissimilar for the lighter fluids. Attempting a larger temperature spread for the O_2/H_2 layers, in order to match the reduced temperature ($T_r \equiv T/T_c$) or the dimensionless temperature difference ($|T_2 - T_1| / T_2$) of the C_7H_{16}/N_2 layers, leads to an excessively large density stratification, as illustrated in Fig. 2(a) which shows ρ_2/ρ_1 over a range of T_1 and T_2 at $p = 100$ and 400 atm.

The effect of the density stratification on the stability of the layer has been investigated using two-dimensional (x_1, x_2) inviscid stability analyses based on the error function mean profiles.[26] The stability curves for the layers in Table 3, duplicated from Ref. 26, are plotted in Fig. 2(b). The increased stability of the O_2/H_2 layers is due mainly to their higher density stratification.

Comparison of DNS results

DNS were carried out for the free stream conditions displayed in Table 3; the cases studied in this paper are listed in Table 4. Details of the computations, including the adequacy of the resolution, are discussed in Refs. 8 and 9. Due to the higher initial density stratification for O_2/H_2 (OH) layers compared to C_7H_{16}/N_2 (HN), an O_2/H_2 layer with same dynamic initial conditions as HN600, including $\text{Re}_0 = 600$, did not reach transition and thus it is not possible to compare transitional results for the two species systems when $\text{Re}_0 = 600$.

Considering the dynamic and thermodynamic initial conditions, several types of comparisons are meaningful, as follows: (1) Layers OH750 and HN600 have the same dynamic initial conditions $\lambda_1/\delta_{\omega,0}$ and F_{3D}, and achieve similar momentum-thickness-based Reynolds number, $\text{Re}_m = \text{Re}_0 \delta_m/\delta_{\omega,0}$ (see definition of δ_m in eq. 16), at transition, $\text{Re}_{m,tr}$. However, they represent different species systems and have different initial conditions for $\rho_2/\rho_1, T_1$ and T_2. (2) Layers HN500 and HN800 represent the same species system, have the same initial $\rho_2/\rho_1, F_{3D}$ and achieve similar $\text{Re}_{m,tr}$. However, they are initially perturbed at different $\lambda_1/\delta_{\omega,0}$. (3) Layers OH500 and HN500 have the same Re_0, but they represent different species systems and have different $\rho_2/\rho_1, \lambda_1/\delta_{\omega,0}, F_{3D}, T_1$ and T_2. (4) Layers OH500 and OH550 represent the same species system, have similar $\rho_2/\rho_1, F_{3D}$ and Re_0, and are both

excited at the most unstable wavelength obtained from the compressible stability analysis; however, they have different T_1 and T_2. Each of these four comparisons should elucidate the effect of some initial conditions and concerted consideration of all these results should indicate which of these parameters most influence helicity.

Global growth and rotational characteristics

A fundamental characteristic of mixing layers is their growth. Although many definitions of growth exist, Cortesi et al.[30] showed that several such measures, including the momentum thickness, are qualitatively similar. Here, we define the momentum thickness as

$$\delta_m = \frac{-1}{(\theta_1 - \theta_2)^2} \int_{-L_{2,min}}^{L_{2,max}} (\theta_2 + \langle \rho u_1 \rangle)(\theta_1 + \langle \rho u_1 \rangle)\, dx_2 \tag{16}$$

with $\theta_1 = \langle \rho u_1 \rangle_{x_2 = L_{2,max}}$ and $\theta_2 = \langle \rho u_1 \rangle_{x_2 = L_{2,min}}$, where $L_{2,min} = -L_2/3$ and $L_{2,max} = 2L_2/3$. While the growth is mostly a consequence of entrainment, the product thickness defined as $\delta_p = \int\int\int_V \rho Y_p dV$ in mass units, where $Y_p = 2\min(Y_1, Y_2)$, is a direct consequence of molecular mixing as also explained by Cortesi et al.[30] $\delta_m/\delta_{\omega,0}$ is illustrated versus the non-dimensional time $t^* = t\Delta U_0/\delta_{\omega,0}$ in Fig. 3(a) for all simulations. All layers roll up and pair twice. However, the C_7H_{16}/N_2 layers display a drastic increase in $\delta_m/\delta_{\omega,0}$ after the first pairing, whereas their O_2/H_2 counterpart tend to grow more slowly. The drastic growth of the C_7H_{16}/N_2 layers compared to the O_2/H_2 ones is attributed to the smaller initial density stratification. This is also the reason that the C_7H_{16}/N_2 layers exhibit a plateau after the second pairing, this being a manifestation of forcing; no such effect is discernible for the more highly-density-stratified O_2/H_2 layers, which are more resistant to entrainment and seem to grow more linearly. Not surprisingly, $\delta_p/\delta_{p,0}$, depicted in Fig. 3(b) displays a much larger growth for C_7H_{16}/N_2 than for O_2/H_2 as a function of t^*, meaning that global molecular mixing is much more intense.

Illustrated in Fig. 3(c) is the non-dimensional positive spanwise vorticity, $\langle\langle \omega_3^+ \rangle\rangle (\delta_{\omega,0}/\Delta U_0)$, which is indicative of small turbulent scale formation considering that due to the initial mean velocity profile, the initial spanwise vorticity is negative. The non-dimensional enstrophy, $\langle\langle \omega_i \omega_i \rangle\rangle (\delta_{\omega,0}/\Delta U_0)^2$, where $\langle\langle\rangle\rangle$ denotes volume averaging, is shown in Fig. 3(d) and is a manifestation of stretching and tilting, which is the mechanism primarily responsible for the formation of small scales. For all simulations, $\langle\langle \omega_3^+ \rangle\rangle (\delta_{\omega,0}/\Delta U_0)$ increases from the null value once the layer roll-up is completed; for each of the set of species, the layer perturbed at the shortest wavelength exhibits the earliest roll-up and highest $\langle\langle \omega_3^+ \rangle\rangle (\delta_{\omega,0}/\Delta U_0)$ maximum growth. Noticeably, the two O_2/H_2 layers perturbed at the most unstable wavelength and having a smaller Re_0 display a de-

layed roll-up with respect to all other layers. Comparing the O_2/H_2 and C_7H_{16}/N_2 layers, one observes a drastically reduced augmentation rate for the former compared to the latter (with particular significance for the OH500 and HN500 layers, which have the same Re_0) indicating a reduced layer growth rate. All curves exhibit local peaks at the first pairing; however, $\langle\langle \omega_3^+ \rangle\rangle (\delta_{\omega,0}/\Delta U_0)$ increases following the first pairing of the C_7H_{16}/N_2 layers but decreases for the O_2/H_2 layers. Moreover, $\langle\langle \omega_3^+ \rangle\rangle (\delta_{\omega,0}/\Delta U_0)$ is considerably smaller for the O_2/H_2 layer compared to the equivalent C_7H_{16}/N_2 ones, indicating that turbulence for the former is substantially reduced with respect to the latter. The enstrophy variation is consistent with this physical picture, displaying reduced levels for the O_2/H_2 layers when compared to the C_7H_{16}/N_2 ones. The largest enstrophy among O_2/H_2 layers corresponds to the one exhibiting the earliest roll-up and maximum positive spanwise vorticity.

Visualizations of the spanwise vorticity, presented in Fig. 4 in the braid plane, show important qualitative differences between the layers. In addition to the vorticity magnitude being lower for O_2/H_2 layers, as previously seen from the global measures, the characteristic scales over which changes in the vorticity occur are evidently larger for the O_2/H_2 layers compared to their C_7H_{16}/N_2 counterpart. These larger length scales were also observed in the density-gradient-magnitude,[8,9] and were attributed to the differences in species-system thermodynamics.

Helicity characteristics

Since the O_2/H_2 and C_7H_{16}/N_2 layers display very different turbulence characteristics, it is of interest to examine how these manifest through the helicity characteristics.

Relative helicity density

Presented in Fig. 5 is the PDF of $\cos(\mathbf{u}, \omega)$ for all simulations listed in Table 4 at the respective transitional states. Clearly, the most likely orientations are orthogonal, positively aligned and negatively aligned. However, the relative likelihood of the three orientations depends on the layers. For OH500 and OH550, negative alignment is most likely, although the three orientations have similar probabilities. For the other four layers, orthogonality is most favored, but is much more strongly favored compared to alignment for the OH750 and HN800 layers. The PDFs of the O_2/H_2 layers are less symmetric than the C_7H_{16}/N_2 ones, particularly when considering the possibility of negative or positive alignment. The O_2/H_2 layers, which are less turbulent than the C_7H_{16}/N_2 layers, further exhibit an increase in the probability of orthogonal $\mathbf{u}$ and ω. Also, favored orthogonality is displayed by layers with combined smaller $\lambda_1/\delta_{\omega,0}$ and larger Re_0, for which larger global spanwise vorticity and enstrophy

were also observed (see Figs. 3(c) and 3(d)). One can conceptually understand that for orthogonal $\mathbf{u}$ and ω, the flow wraps around vortex tubes and turbulence may be enhanced, thereby presenting a consistent picture with the global layer evolution results. For the mixing layers here studied, the results are that either alignment or orthogonality of $\mathbf{u}$ and ω is the most likely orientation, but typically most of the flow region exhibits no correlation between the $\mathbf{u}$ and ω orientations. Thus, the diverse alignment features found in previous studies[13-17] are displayed by supercritical mixing layers, according to the different systems of species and different initial conditions.

Helicity density at transitional states

To understand the characteristics of $(\mathbf{u} \cdot \omega)$ at the transitional states, illustrations of $(\mathbf{u} \cdot \omega)\delta_{\omega,0}/(\Delta U_0)^2$ homogeneous (x_1, x_3)-plane averages and root-mean-squares (RMS) appear in Fig. 6. The average $(\mathbf{u} \cdot \omega)$ (Fig. 6(a)) has both positive and negative regions, showing a complex flow field. For the RMS (Fig. 6(b)), all layers have a peak in the lighter fluid side ($x_2 > 0$), although HN500 and HN800 have an additional peak in the heavier fluid and a trough in the middle of the layer. The $(\mathbf{u} \cdot \omega)$ RMS activity is mostly on the lighter fluid side for the O_2/H_2 layers perturbed at the most unstable wavelength, but as $\lambda_1/\delta_{\omega,0}$ decreases and Re_0 concomitantly increases, the fluctuation activity narrows and moves towards the heavier fluid, indicating that these conditions are more effective at increasing $(\mathbf{u} \cdot \omega)$ in the heavier fluid. A similar trend is seen for the C_7H_{16}/N_2 layers, and at the shortest estimated $\lambda_1/\delta_{\omega,0}$ and largest Re_0, the high RMS activity region is almost centered on the center-line of the layer. Accompanying this translation of the activity region towards the heavier fluid, one observes an increase in the maximum RMS of the layers. The relative RMS magnitude of the layers generally matches that of $\langle\langle\omega_i\omega_i\rangle\rangle (\delta_{\omega,0}/\Delta U_0)$.

Three-dimensional visualizations (not shown) reveal that all layers are dominated by streamwise tubes of high vorticity magnitude that tend to map the edges of the coherent vortices, and the dominant contributions to $(\mathbf{u} \cdot \omega)$ occur where these tubes lie in high velocity regions. Due to the initial conditions, adjacent vortex tubes have opposite sign but similar magnitude of streamwise vorticity, with corresponding behavior of $(\mathbf{u}\cdot\omega)$. This leads to the RMS $(\mathbf{u}\cdot\omega)$ being much larger than the average, both on planar and a volumetric basis; the helicity density volumetric average and RMS are tabulated in Table 5. For all layers except HN800, $(\mathbf{u}\cdot\omega)$ average is negative. The magnitude of the average is a factor of two larger for the O_2/H_2 layers than for the C_7H_{16}/N_2 layers, yet the opposite behavior is observed for the RMS. This suggests stronger symmetry between the streamwise tubes for the C_7H_{16}/N_2 layers, consistent with the more symmetric PDFs in

Fig. 5. Among C_7H_{16}/N_2 layers, the largest fluctuations are displayed by HN800 and the smallest by HN500. Comparing HN500 and HN600, it is inferred that the $(\mathbf{u} \cdot \omega)$ fluctuations increase with Re_0 at otherwise same initial conditions. However, at same Re_0, the C_7H_{16}/N_2 layer exhibits about twice as much RMS as its O_2/H_2 counterpart, which is attributed to the thermodynamic differences between the two systems as well as to the differences in the other (than Re_0) initial conditions.

Helicity density evolution

To investigate the contributions to the changes in $(\mathbf{u} \cdot \omega)$ for each layer at the transitional states, we calculated the $(\mathbf{u} \cdot \omega)$ budget from

$$
\begin{aligned}
\frac{D}{Dt}(\mathbf{u} \cdot \omega) = {} & \omega \cdot \nabla \left(\frac{1}{2}\mathbf{u} \cdot \mathbf{u}\right) - (\mathbf{u} \cdot \omega)(\nabla \cdot \mathbf{u}) \\
& - \mathbf{u} \cdot \left[\nabla \times \left(\frac{1}{\rho}\nabla p\right)\right] - \omega \cdot \left(\frac{1}{\rho}\nabla p\right) \\
& + \mathbf{u} \cdot \left[\nabla \times \left(\frac{1}{\rho}\nabla \cdot \bar{\bar{\tau}}\right)\right] + \omega \cdot \left(\frac{1}{\rho}\nabla \cdot \bar{\bar{\tau}}\right),
\end{aligned}
\tag{17}
$$

We note that for the incompressible flows that have been the subject of most $(\mathbf{u} \cdot \omega)$ studies, the dilatation $(\nabla \cdot \mathbf{u})$ is null, and if the density is constant, the baroclinic term $(\nabla \times (\nabla p/\rho) = \nabla (1/\rho) \times (\nabla p))$ is additionally null.

The homogeneous (x_1, x_3)-plane contributions to $D(\mathbf{u} \cdot \omega)/Dt$ budgets are illustrated in Figs. 7 and 8. Considering both the averages (Fig. 7) and the RMS (Fig. 8), we note that contributions from the dilatation and vorticity-stress terms are much smaller than those from the other four terms. Average contributions from different terms tend to be larger for the C_7H_{16}/N_2 when compared to the O_2/H_2 layers, indicating an increased activity in most effects responsible for $(\mathbf{u} \cdot \omega)$ production. This trend is more pronounced for the RMS, where the contributions of C_7H_{16}/N_2 layers tend to be almost an order of magnitude larger than those for their O_2/H_2 counterpart, indicating a much larger activity in the former. Some of this increased activity can be traced to the smaller length scales of the C_7H_{16}/N_2 layers, observed in the vorticity contour plots of Fig. 4, which would result in larger gradients. Generally, $\omega \cdot \nabla \left(\frac{1}{2}\mathbf{u} \cdot \mathbf{u}\right)$ seems to be the most crucial mechanism for $(\mathbf{u}\cdot\omega)$ creation. The scalar product of the vorticity with the pressure gradient appears to be the second most important mechanism for $(\mathbf{u}\cdot\omega)$ activity, confirming that thermodynamic effects are important in $(\mathbf{u} \cdot \omega)$ production in supercritical turbulence. Noteworthy, it seems that $(\mathbf{u} \cdot \omega)$ is not self-perpetuating in that it does not produce, through the dilatation term, effects that will tend to enhance itself. With decreasing $\lambda_1/\delta_{\omega,0}$ and concomitantly increasing Re_0, the activity of all terms increases and a

cross-stream location of minimal RMS activity develops in some (e.g. OH750) or all (e.g. HN800) terms of eq. 17. This location of minimal RMS activity is in the vicinity to the local trough identified in the RMS of $(\mathbf{u} \cdot \omega)$.

Consideration of the volume integral of eq. 17 in conjunction with the assumption that boundary terms are negligible (assumption checked for all databases, and found to be excellent), leads to

$$\int_V \frac{\partial (\mathbf{u} \cdot \omega)}{\partial t} dV = \int_V 2\mathbf{u} \cdot \left[\nabla \times \left(-\frac{1}{\rho} \nabla p + \frac{1}{\rho} \nabla \cdot \bar{\bar{\tau}} \right) \right] dV. \tag{18}$$

Eq. 18 demonstrates that any changes in H can be attributed to baroclinic and viscous effects, consistent indeed with Moffatt.[11] The additional implication here is that while generally H is considered to be a dynamic characteristic of the flow, in the present situation, it depends on the thermodynamics through its association with the EOS embedded in ∇p. For all layers, examination of the budget of eq. 18 at transition shows that the viscous term has the opposite sign of the baroclinic term; the volume average of the terms (i.e. terms divided by $2V$) is presented in Table 6. The HN800 is distinct from the other layers in that its viscous term is negative. For four cases, the magnitude of the viscous term is larger than that of the baroclinic term. The two cases where the magnitude of the baroclinic term is larger are OH550 and HN500 (10% and 70% larger, respectively). No clear trend with species system, or with Re_0 and $\lambda_1/\delta_{\omega,0}$, emerges in the absolute or relative magnitudes of the baroclinic and viscous terms. This highlights the importance of the thermodynamics under supercritical conditions as rivaling viscous contributions to the helicity evolution.

Finally, illustrations of the helicity, normalized by its initial value (H_0), calculated from the DNS databases, are shown in Fig. 9(a) as a function of t^* for all layers listed in Table 4. All layers exhibit strong H/H_0 non-monotonicity, which is attributed to the complex entrainment and mixing process. Clearly, for the C_7H_{16}/N_2 layers, H/H_0 begins increasing from its original value following roll-up, and each of the pairings corresponds to either a local or global minimum in H/H_0. In contrast, no such correspondence is detected for the O_2/H_2 layers where H/H_0 remains approximately constant well past the second pairing and variations occur only late in the evolution of the layers. Comparisons of $\langle\langle \mathbf{u} \cdot \omega \rangle\rangle \delta_{\omega,0}/(\Delta U_0)^2$, where $\langle\langle \mathbf{u} \cdot \omega \rangle\rangle = H/V$, between the two layer types (Fig. 9(b)) show that its magnitude is generally larger for the C_7H_{16}/N_2 layers. These findings are consonant with the decreased turbulence level of the O_2/H_2 layers compared to their C_7H_{16}/N_2 counterpart, which were traced to thermodynamic effects. Also, $\langle\langle \mathbf{u} \cdot \omega \rangle\rangle \delta_{\omega,0}/(\Delta U_0)^2$ is larger for the layers with the smaller $\lambda_1/\delta_{\omega,0}$ and larger Re_0, independent of the species system.

Summary and conclusions

The helicity characteristics of supercritical turbulent mixtures were investigated on databases obtained from Direct Numerical Simulations. The simulations are of three-dimensional binary-species temporal mixing layers, in which each stream is initially composed of a single species. The two species systems investigated were O_2/H_2 and C_7H_{16}/N_2, and the initial conditions were such that all results are from simulations performed at similar momentum ratios and at approximately the same reduced pressure of 2 with respect to the pure heavier species. The layer is initially perturbed to initiate entrainment, roll-up and pairing. Each layer originally consists of four spanwise vortices, which undergo two pairings to form a single ultimate vortex within which small scales proliferate; eventually a transitional state is reached by each layer. The database used in this study consisted of three simulations of each O_2/H_2 and C_7H_{16}/N_2 layers, with the initial conditions for the same binary species system differing by the initial vorticity-thickness-based Reynolds number, the initial-perturbation wavelength and the amplitude of the initial streamwise vorticity.

Global characteristics of the six layers showed that the momentum thickness and product thickness growth is substantially reduced for the O_2/H_2 layers compared to the C_7H_{16}/N_2 ones. This result is attributed to the much larger initial density stratification of the former layers, which delays entrainment and pairing. The global positive spanwise vorticity indicated that the turbulence level of O_2/H_2 layers is less than that of comparable C_7H_{16}/N_2 layers.

Examination of the helicity characteristics of the layers showed that velocity and vorticity are most likely orthogonal or aligned, with spatially localized high helicity density. Both the relative helicity density and the helicity density were less symmetrically distributed between negative and positive values for the O_2/H_2 layers, and the helicity density activity was also less intense. The governing mechanism for helicity-density creation at transition is the coupling of the kinetic energy gradient and the vorticity, followed by the interaction of the vorticity with the pressure gradient. The helicity varies non-monotonically during the evolution of the flow; these variations were traced to the balance between baroclinic and viscous effects. The species-system dependent aspects of the relative helicity density and the influence of the pressure gradient on the helicity evolution indicate that for supercritical mixing layers, thermodynamic effects play an important role in generating helicity.

Acknowledgements

References

[1]Prausnitz, J., Lichtenthaler, R., and de Azevedo, E., *Molecular Thermodynamics for Fluid-Phase Equilibrium*, Prentice-Hall, 1986.

[2]Hirshfelder, J., Curtis, C., and Bird, R., *Molecular Theory of Gases and Liquids*, John Wiley and Sons, 1964.

[3]Chehroudi, B., Talley, D., and Coy, E., "Initial Growth Rate and Visual Characteristics of a Round Jet Into a Sub- to Supercritical Environment of Relevance to Rocket, Gas Turbine and Diesel Engines," AIAA 99-0206, 1999, AIAA 37th Aerospace Sciences Meeting and Exhibit, Reno, NV, Jan. 11-14.

[4]Mayer, W., Schik, A., Schweitzer, C., and Schaffler, M., "Injection and Mixing Processes in High Pressure LOX/GH2 Rocket Combustors," AIAA 96-2620, 1996, AIAA/ASME/SAE/ASEE 32nd Joint Propulsion Conference, Lake Buena Vista, FL, July 1-3.

[5]Mayer, W., Ivancic, B., Schik, A., and Hornung, U., "Propellant Atomization in LOX/GH2 Rocket Combustors," AIAA 98-3685, 1998, AIAA/ASME/SAE/ASEE 34th Joint Propulsion Conference and Exhibit, Cleveland, OH, July 13-15.

[6]Oschwald, M. and Schik, A., "Supercritical Nitrogen Free Jet Investigated by Spontaneous Raman Scattering," *Experiments in Fluids*, Vol. 27, 1999, pp. 497–506.

[7]Miller, R., Harstad, K., and Bellan, J., "Direct Numerical Simulations of Supercritical Fluid Mixing Layers Applied to Heptane-Nitrogen," *Journal of Fluid Mechanics*, Vol. 436, 2001, pp. 1–39.

[8]Okong'o, N. and Bellan, J., "Direct Numerical Simulation of a Transitional Supercritical Binary Mixing Layer: Heptane and Nitrogen," *Journal of Fluid Mechanics*, Vol. 464, 2002, pp. 1–34.

[9]Okong'o, N., Harstad, K., and Bellan, J., "Direct Numerical Simulations of O_2/H_2 Temporal Mixing Layers Under Supercritical Conditions," *AIAA Journal*, Vol. 40, No. 5, May 2002, pp. 914–926.

[10]Bellan, J., "Supercritical (and Subcritical) Fluid Behavior and Modeling: Drops, Streams, Shear and Mixing Layers, Jets and Sprays," *Progress in Energy and Combustion Science*, Vol. 26, No. 4–6, 2000, pp. 329–366.

[11]Moffatt, H. K., "The Degree of Knottedness of Tangle Vortex Lines," *Journal of Fluid Mechanics*, Vol. 35, 1969, pp. 117–129.

[12]Moffatt, H. K., "Helicity in Laminar and Turbulent Flows," *Annual Reviews of Fluid Mechanics*, Vol. 24, 1992, pp. 281–312.

[13]Shtilman, L., Pelz, R., and Tsinober, A., "Numerical Investigation of Helicity in Turbulent Flow," *Computers & Fluids*, Vol. 16, No. 3, 1988, pp. 341–347.

[14]Rogers, M. M. and Moin, P., "Helicity Fluctuations in Incompressible Turbulent Flows," *Physics of Fluids*, Vol. 30, No. 9, September 1987, pp. 2662–2671.

[15]Pelz, R. and Shtilman, L. and Tsinober, A., "The Helical Nature of Unforced Turbulent Flows," *Physics of Fluids*, Vol. 29, No. 11, November 1986, pp. 3506–3508.

[16]Pelz, R., Yakhot, V., and Orszag, S., "Velocity-Vorticity Patterns in Turbulent Flow," *Physical Review Letters*, Vol. 54, No. 23, June 1985, pp. 2505–2508.

[17]Wallace, J., Balint, J.-L., and Ong, L., "An Experimental Study of Helicity Density in Turbulent Flows," *Physics of Fluids A*, Vol. 4, No. 9, September 1992, pp. 2013–2026.

[18]Keizer, J., *Statistical Thermodynamics of Nonequilibrium Processes*, Springer-Verlag, New York, 1987.

[19]Sarman, S. and Evans, D., "Heat Flux and Mass Diffusion in Binary Lennard-Jones Mixtures," *Physics Review A*, Vol. 45, No. 4, 1992, pp. 2370–2379.

[20]Harstad, K. and Bellan, J., "An All-Pressure Fluid-Drop Model Applied to a Binary Mixture: Heptane in Nitrogen," *International Journal of Multiphase Flow*, Vol. 26, No. 10, 2000, pp. 1675–1706.

[21]Harstad, K., Miller, R., and Bellan, J., "Efficient High Pressure State Equations," *AICHE Journal*, Vol. 43, No. 6, 1997, pp. 1605–1610.

[22]Harstad, K. and Bellan, J., "Isolated Fluid Oxygen Drop Behavior in Fluid Hydrogen at Rocket Chamber Pressures," *International Journal of Heat and Mass Transfer*, Vol. 41, 1998, pp. 3537–3550.

[23]Papamoschou, D. and Roshko, A., "The Compressible Turbulent Shear Layer: An Experimental Study," *Journal of Fluid Mechanics*, Vol. 197, 1988, pp. 453–477.

[24]Moser, R. and Rogers, M., "Mixing Transition and the Cascade to Small Scales in a Plane Mixing Layer," *Physics of Fluids A*, Vol. 3, No. 5, 1991, pp. 1128–1134.

[25]Moser, R. and Rogers, M., "The Three-Dimensional Evolution of a Plane Mixing Layer: Pairing and Transition to Turbulence," *Journal of Fluid Mechanics*, Vol. 247, 1993, pp. 275–320.

[26]Okong'o, N. and Bellan, J., "Real gas effects on mean flow and temporal, inviscid linear stability of binary-species mixing layers," to be submitted to *AIAA Journal*.

[27]Okong'o, N. and Bellan, J., "Consistent Boundary Conditions for Multicomponent Real Gas Mixtures Based on Characteristic Waves," *Journal of Computational Physics*, Vol. 176, 2002, pp. 330–344.

[28]Kennedy, C. and Carpenter, M., "Several New Numerical Methods for Compressible Shear Layer Simulations," *Applied Numerical Mathematics*, Vol. 14, 1994, pp. 397–433.

[29]Muller, S. M. and Scheerer, D., "A Method to Parallelize Tridiagonal Solvers," *Parallel Computing*, Vol. 17, 1991, pp. 181–188.

[30]Cortesi, A., Smith, B., Yadigaroglu, G., and Banerjee, S., "Numerical Investigation of the Entrainment and Mixing Processes in Neutral and Stably-Stratified Mixing Layers," *Physics of Fluids*, Vol. 11, No. 1, January 1999, pp. 162–185.

[31]Harstad, K. and Bellan, J., "The D^2 Variation For Isolated LOX Drops and Polydisperse Clusters in Hydrogen at High Temperature and Pressures," *Combustion and Flame*, Vol. 124, 2001, pp. 535–550.

Species	m (g/mol)	T_c (K)	p_c(MPa)	v_c(cm^3/mol)
H_2	2.016	33.0	1.284	64.3
N_2	28.013	126.3	3.399	89.8
O_2	31.999	154.6	5.043	73.4
C_7H_{16}	100.205	540.2	2.74	432.0

Table 1   Pure species properties; v_c is the molar volume at the critical point.

System	C_7H_{16}/N_2	O_2/H_2
$\mu = \mu_R \left(T/T_R\right)^n$	$n = 0.7$	$n = 0.75$
$Sc \equiv \mu/\left(\rho \alpha_D D\right)$	$1.5 - Y_h$	$\left(1.334 - 0.668 Y_O - 0.186 Y_O^2 - 0.268 Y_O^6\right)\left[1 + (88.6/T)^{1.5}\right]$
$Pr \equiv \mu C_p/\left(m\lambda\right)$	$0.5 Sc/\exp\left(-1.5 Y_h\right)$	$1.335/T^{0.1}$
α_{IK} or α_{BK}	$\alpha_{IK} = 0.1$ (Ref. 20)	$\alpha_{BK} = 0.2$ (Refs. 22,31)
T Range	500K–1100K	200K–800K
p Range	40 atm–80 atm	$\sim$100atm

Table 2   Transport properties for binary mixtures. The reference temperature is $T_R = (T_1 + T_2)/2$, T in Kelvin; Y_O is the O_2 mass fraction, Y_h is the C_7H_{16} mass fraction.

	$\rho_2/\rho_1 = 12.88$		$\rho_2/\rho_1 = 24.40$		$\rho_2/\rho_1 = 24.51$	
Stream	C_7H_{16}	N_2	O_2	H_2	O_2	H_2
u_1(m/s)	-85.947	209.856	-158.004	770.983	-114.926	568.972
a_s(m/s)	181.327	643.709	397.517	1915.376	295.985	1381.95
ρ(kg/m^3)	259.487	20.141	96.764	3.965	197.317	8.050
p_0(atm)	60	60	100	100	100	100
T(K)	600	1000	400	600	235	287
Y_2	1	0	1	0	1	0
Z	0.4706	1.017	1.008	1.033	0.841	1.063
$p_r = p/p_c$	2.22	1.81	2.01	7.89	2.01	7.89
$\Delta U_0 = U_1 - U_2$	295.80		928.99		683.90	
$\lvert\rho_2 U_2\rvert / \lvert\rho_1 U_1\rvert$	5.276		5.001		4.951	

Table 3   Mean flow properties for various mixing layers; $M_{c,0} = 0.4$.

Run	Re_0	ρ_2/ρ_1	$\lambda_1/\delta_{\omega,0}$	F_{3D}	$L_1 \times L_2 \times L_3$	$N_1 \times N_2 \times N_3$	$Re_{m,tr}$	t_{tr}^*	CPU(h)
OH500	500	24.51	10.61	0.025	0.291×0.291×0.1746	352×352×208	1772	290	14557
OH550	550	24.40	10.35	0.025	0.284×0.284×0.17	352×352×208	1907	270	14497
OH750	750	24.40	7.29	0.05	0.2×0.2×0.12	352×352×208	1507	150	10349
HN500	500	12.88	7.29	0.05	0.2×0.232×0.12	240×288×144	1250	155	1714
HN600	600	12.88	7.29	0.05	0.2×0.232×0.12	288×336×176	1452	135	5156
HN800	800	12.88	4.57	0.05	0.125×0.148×0.075	240×272×144	1258	100	1916

Table 4   Listing of the simulations and associated resolution for O_2/H_2 (OH) and C_7H_{16}/N_2 (HN) mixing layers. L_i is in meters. For all layers, $L_1=4\lambda_1$, $\delta_{\omega,0}=6.859\times10^{-3}$ m and $F_{2D}=0.1$. The other initial conditions are listed in Table 3 under the value of ρ_2/ρ_1. The subscript tr denotes the transitional time. The CPU time is based on an SGI Origin2000 300MHz R12000 processor.

Run	Average	RMS
OH500	-4.6152×10^{-4}	2.0858×10^{-2}
OH550	-2.0422×10^{-4}	2.1258×10^{-2}
OH750	-3.3391×10^{-4}	1.9367×10^{-2}
HN500	-1.4288×10^{-4}	3.7422×10^{-2}
HN600	-1.0542×10^{-4}	4.2618×10^{-2}
HN800	+1.9679×10^{-4}	5.3249×10^{-2}

Table 5 $(\mathbf{u} \cdot \omega)\,\delta_{\omega,0}/\left(\Delta U_0\right)^2$, volumetric average and RMS.

Run	$-\mathbf{u} \cdot \left[\nabla \times \left(\frac{1}{\rho}\nabla p\right)\right]$	$\mathbf{u} \cdot \left[\nabla \times \left(\frac{1}{\rho}\nabla \cdot \overline{\overline{\tau}}\right)\right]$
OH500	-2.6149×10^{-6}	8.4336×10^{-6}
OH550	-2.3121×10^{-6}	2.0947×10^{-6}
OH750	-8.7586×10^{-7}	1.3953×10^{-6}
HN500	-5.2068×10^{-6}	3.1886×10^{-6}
HN600	-2.0605×10^{-6}	1.4284×10^{-5}
HN800	2.6484×10^{-6}	-1.1767×10^{-5}

Table 6   Contributions to $D\left(\mathbf{u} \cdot \omega\right)/Dt$, normalized by $\left(\delta_{\omega,0}\right)^2/\left(\Delta U_0\right)^3$, volumetric average.
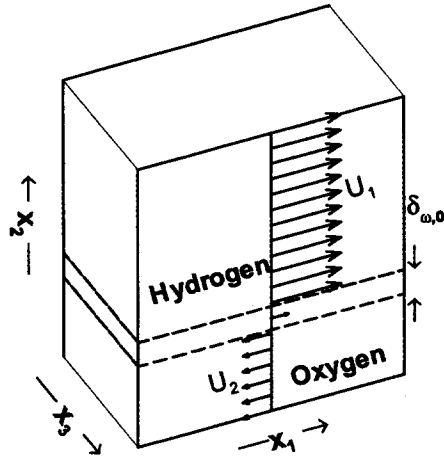
Fig. 1   Sketch of the O_2/H_2 mixing layer configuration.

(a)

(b)
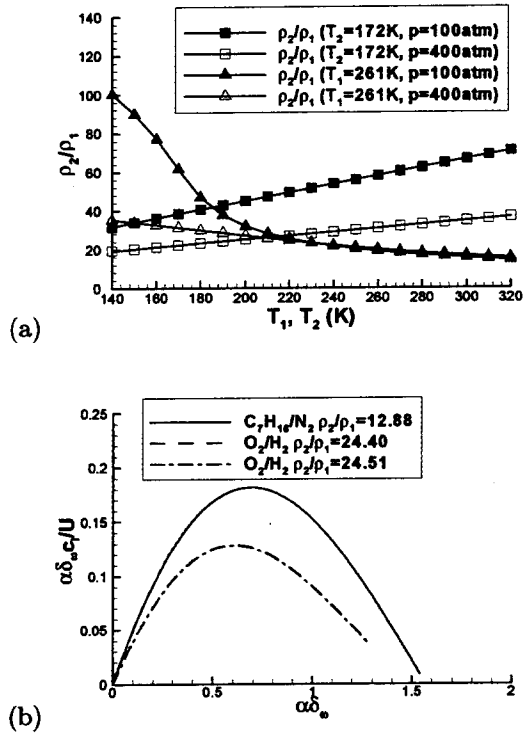
Fig. 2   (a) ρ_2/ρ_1 versus T_1 and T_2 for O_2/H_2 at different conditions (b) Comparison of the stability curves for C_7H_{16}/N_2 and O_2/H_2 for $\rho_2/\rho_1 = 1$ and 12.88.
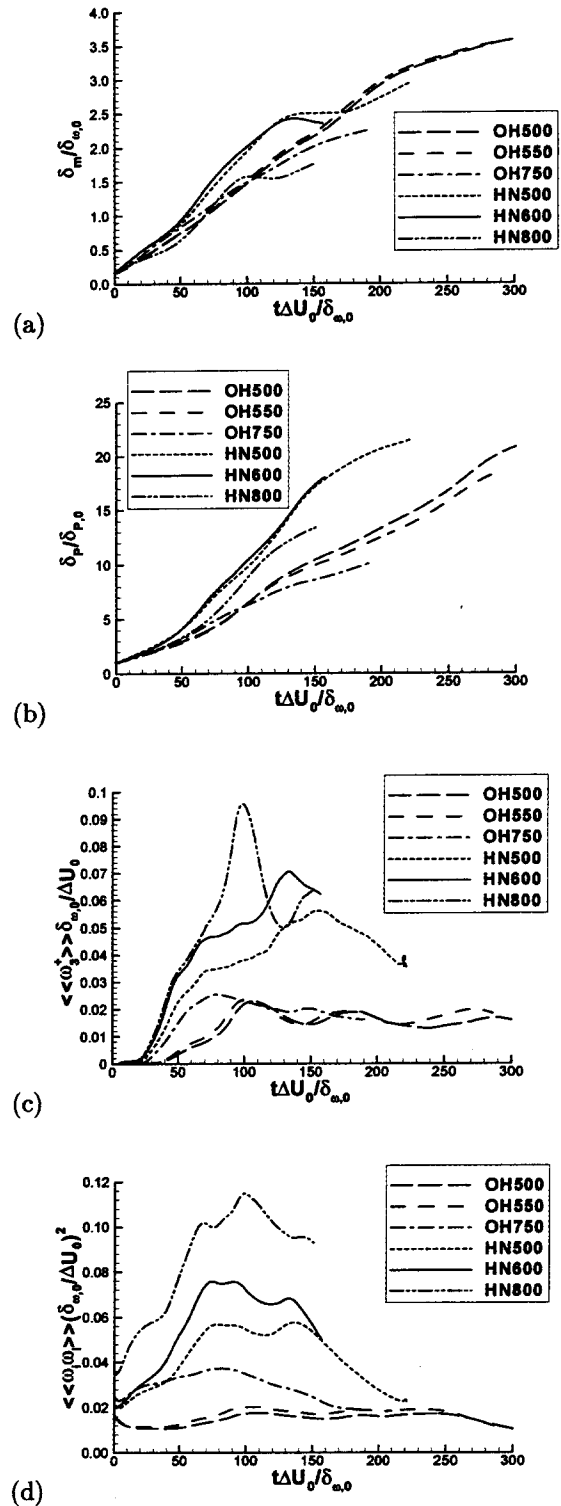

(a)

(b)

(c)

(d)

Fig. 3   Non-dimensionalized (a) momentum thickness, (b) product thickness, (c) global positive spanwise vorticity, and (d) enstrophy, all versus $t^* = t/(\Delta U_0/\delta_{\omega,0})$.
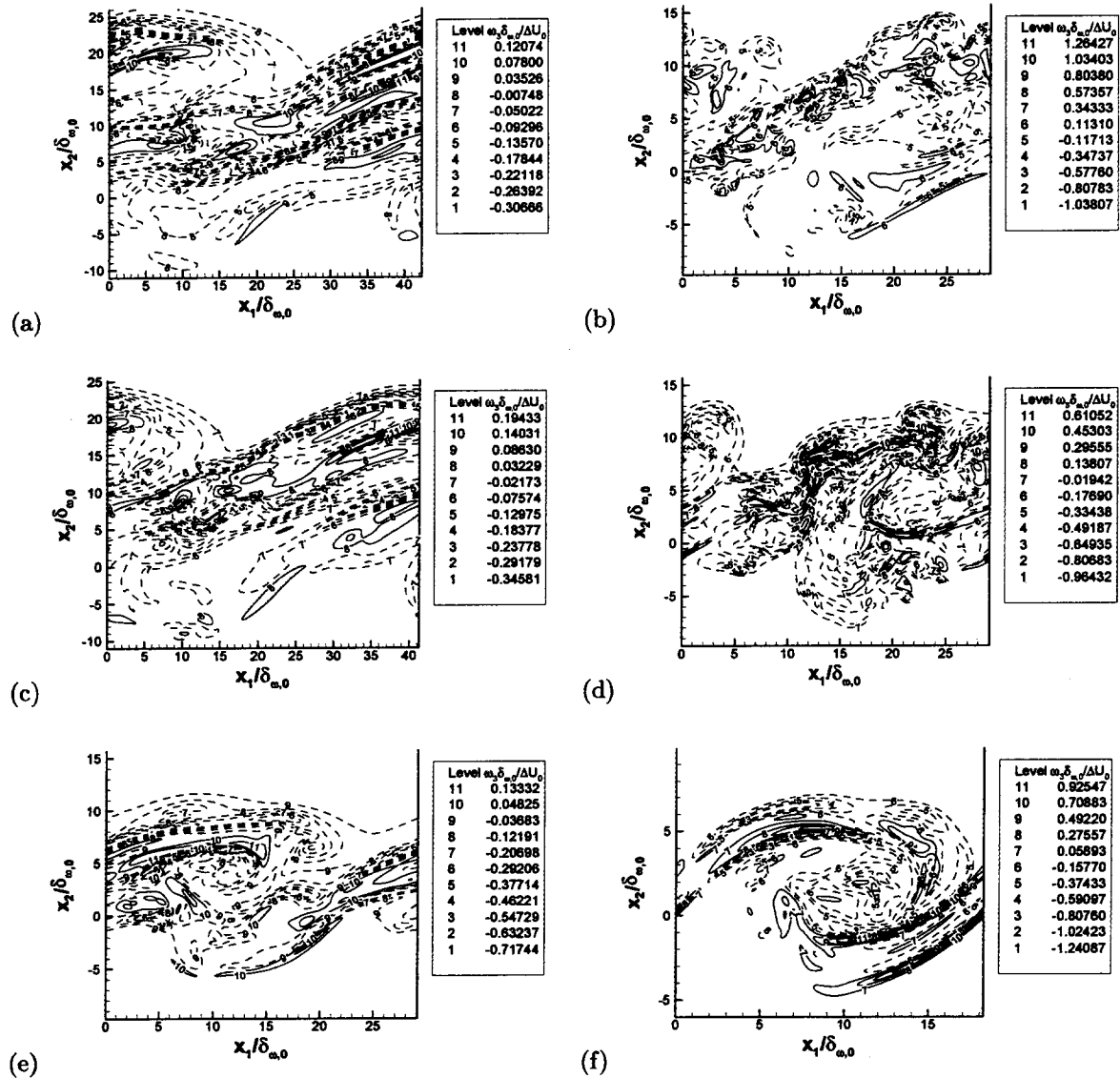
Fig. 4 Spanwise vorticity for (a) OH500, (b) HN500, (c) OH550, (d) HN600, (e) OH750 and (f) HN800: in the braid plane ($x_3 = L_3/16$) at the transitional time.
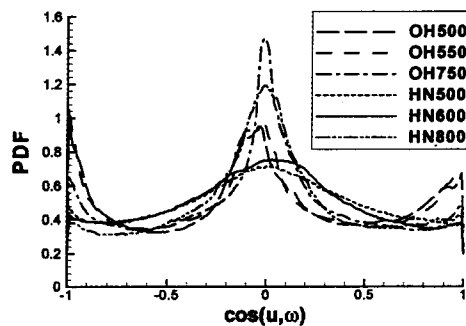

Fig. 5 Probability density function of $\cos(u, \omega)$ for all layers listed in Table 4, at the respective transitional states .
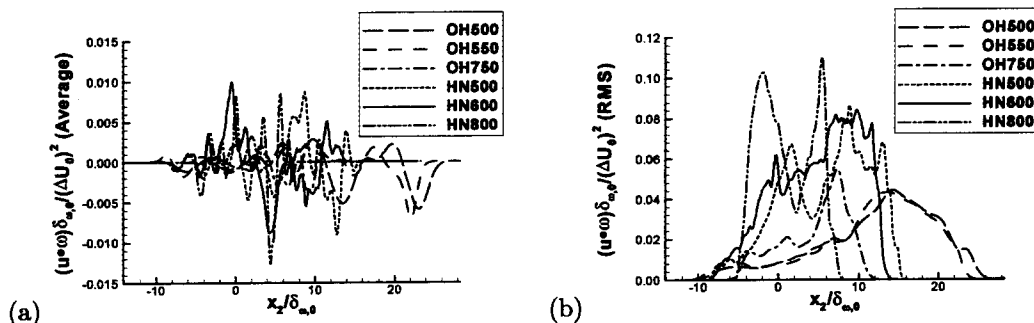
AMERICAN INSTITUTE OF AERONAUTICS AND ASTRONAUTICS PAPER 2003-0481

Fig. 6 $(\mathbf{u} \cdot \omega)$: (a) average and (b) RMS in (x_1, x_3) planes, at the transitional states.

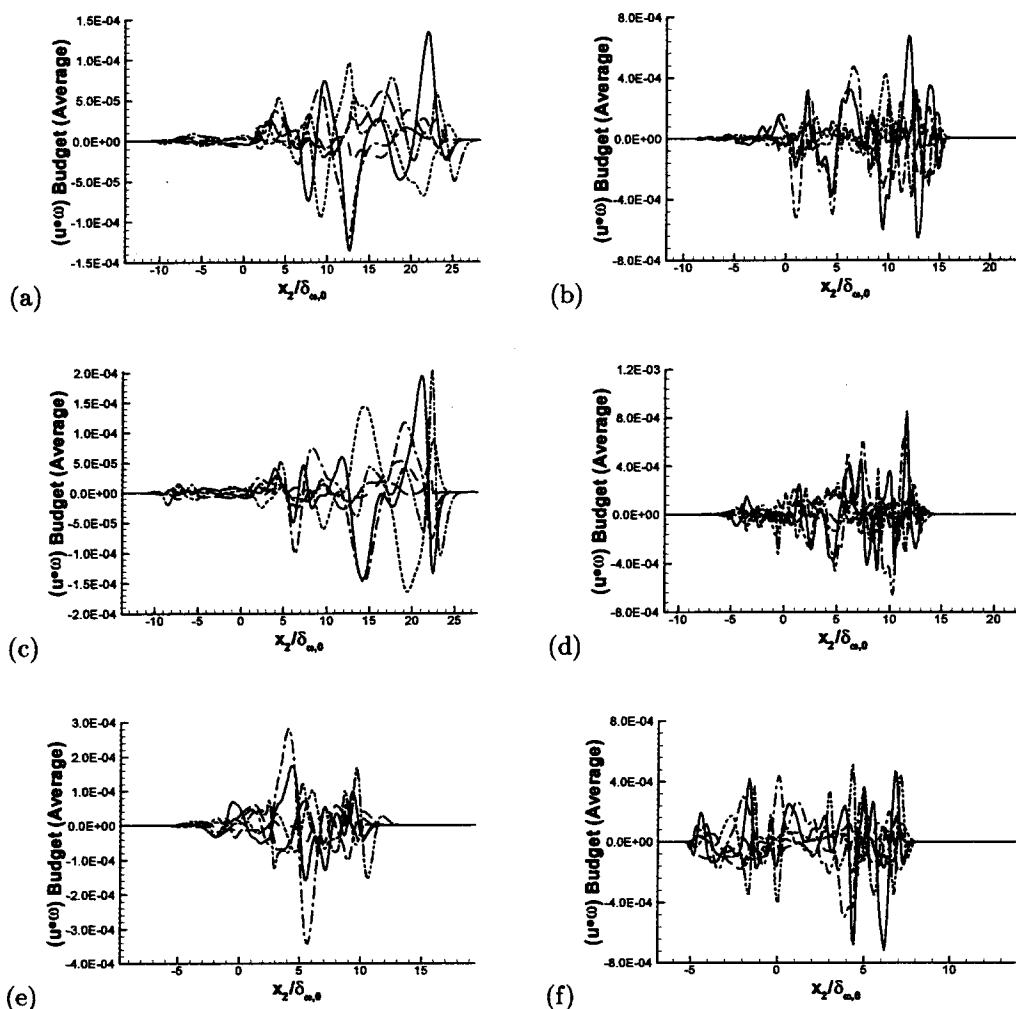|		
——————	$\omega \cdot \nabla \left(\frac{1}{2} u \cdot u\right) \left[\left(\delta_{\omega,0}\right)^2 / \left(\Delta U_0\right)^3\right]$	············ $-u \cdot \{\nabla \times [(1/\rho)\, \nabla p]\} \left[\left(\delta_{\omega,0}\right)^2 / \left(\Delta U_0\right)^3\right]$
— — — —	$-(u \cdot \omega)(\nabla \cdot u) \left[\left(\delta_{\omega,0}\right)^2 / \left(\Delta U_0\right)^3\right]$	— — — — $\omega \cdot [(1/\rho)(\nabla \cdot \tau)] \left[\left(\delta_{\omega,0}\right)^2 / \left(\Delta U_0\right)^3\right]$
— · — · —	$-\omega \cdot [(1/\rho)\, \nabla p] \left[\left(\delta_{\omega,0}\right)^2 / \left(\Delta U_0\right)^3\right]$	— ·· — ·· — $u \cdot \{\nabla \times [(1/\rho)(\nabla \cdot \tau)]\} \left[\left(\delta_{\omega,0}\right)^2 / \left(\Delta U_0\right)^3\right]$

Fig. 7   Budget of $D/Dt\,(\mathbf{u} \cdot \omega)$ at the respective transitional states for (a) OH500, (b) HN500, (c) OH550, (d) HN600, (e) OH750 and (f) HN800: averages in (x_1, x_3) planes.
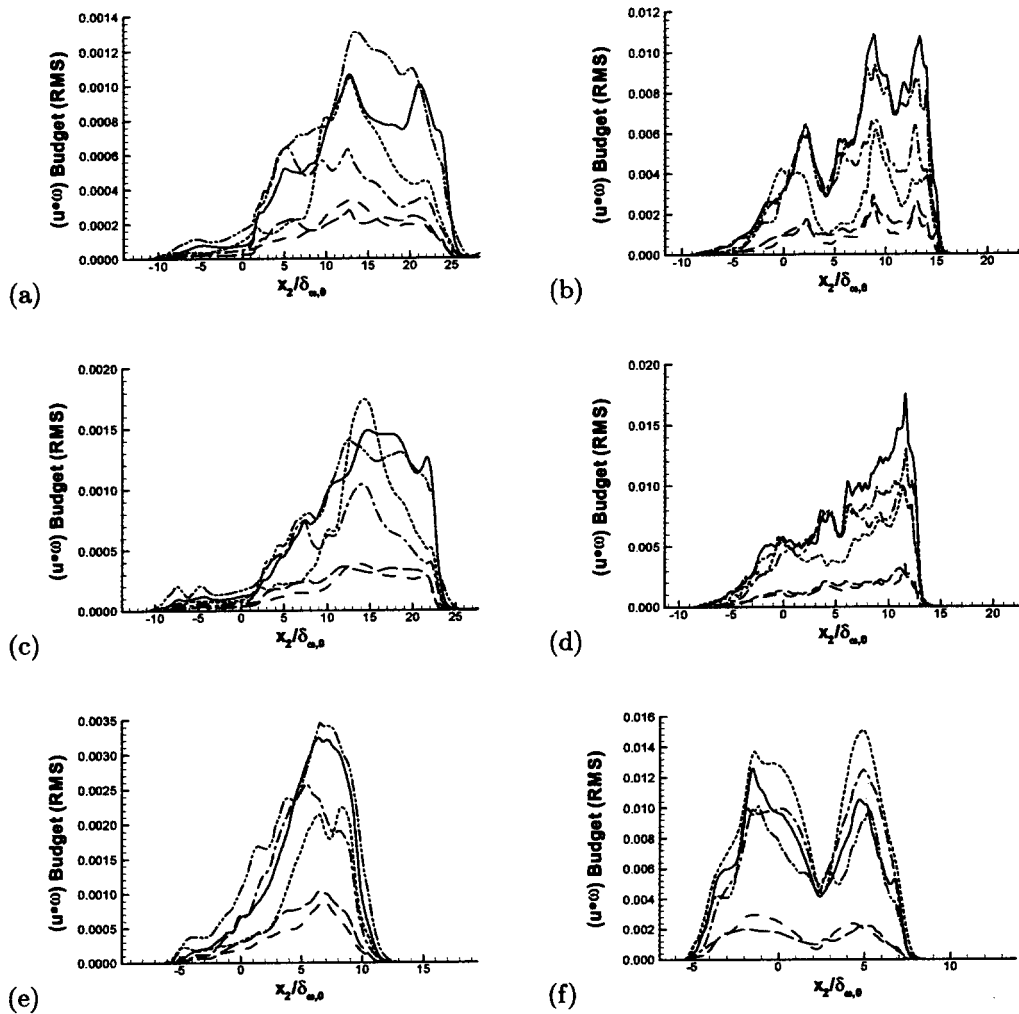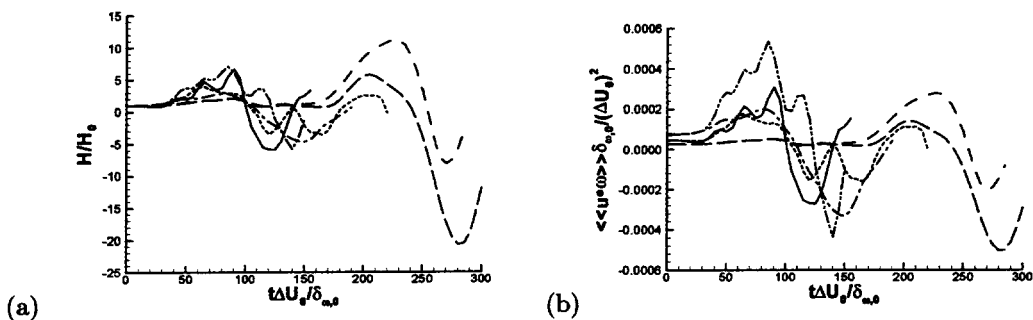
Fig. 8   As for Fig. 7: RMS in (x_1, x_3) planes.

Fig. 9   Helicity evolution. See Fig. 3 for legend.